

MODELING & SIMULATION FOR PARTICLE RADIATION DAMAGE TO ELECTRONIC AND OPTO-ELECTRONIC DEVICES

Sanjay Krishna

**University of New Mexico
1700 Lomas Blvd. NE
Albuquerque, NM 87106**

25 Jan 2018

Final Report

APPROVED FOR PUBLIC RELEASE; DISTRIBUTION IS UNLIMITED.



**AIR FORCE RESEARCH LABORATORY
Space Vehicles Directorate
3550 Aberdeen Ave SE
AIR FORCE MATERIEL COMMAND
KIRTLAND AIR FORCE BASE, NM 87117-5776**

DTIC COPY NOTICE AND SIGNATURE PAGE

Using Government drawings, specifications, or other data included in this document for any purpose other than Government procurement does not in any way obligate the U.S. Government. The fact that the Government formulated or supplied the drawings, specifications, or other data does not license the holder or any other person or corporation; or convey any rights or permission to manufacture, use, or sell any patented invention that may relate to them.

This report is the result of contracted fundamental research which is exempt from public affairs security and policy review in accordance with AFI 61-201, paragraph 2.3.5.1. This report is available to the general public, including foreign nationals. Copies may be obtained from the Defense Technical Information Center (DTIC) (<http://www.dtic.mil>).

AFRL-RV-PS-TR-2018-0001 HAS BEEN REVIEWED AND IS APPROVED FOR
PUBLICATION IN ACCORDANCE WITH ASSIGNED DISTRIBUTION STATEMENT.

//SIGNED//
CHRISTIAN MORATH
Program Manager

//SIGNED//
DAVID CARDIMONA
Technical Advisor, Space Based Advanced Sensing
and Protection

//SIGNED//
JOHN BEAUCHEMIN
Chief Engineer, Spacecraft Technology Division
Space Vehicles Directorate

This report is published in the interest of scientific and technical information exchange, and its publication does not constitute the Government's approval or disapproval of its ideas or findings.

Approved for public release; distribution is unlimited.

REPORT DOCUMENTATION PAGE				Form Approved OMB No. 0704-0188	
Public reporting burden for this collection of information is estimated to average 1 hour per response, including the time for reviewing instructions, searching existing data sources, gathering and maintaining the data needed, and completing and reviewing this collection of information. Send comments regarding this burden estimate or any other aspect of this collection of information, including suggestions for reducing this burden to Department of Defense, Washington Headquarters Services, Directorate for Information Operations and Reports (0704-0188), 1215 Jefferson Davis Highway, Suite 1204, Arlington, VA 22202-4302. Respondents should be aware that notwithstanding any other provision of law, no person shall be subject to any penalty for failing to comply with a collection of information if it does not display a currently valid OMB control number. PLEASE DO NOT RETURN YOUR FORM TO THE ABOVE ADDRESS.					
1. REPORT DATE (DD-MM-YYYY) 25-01-2018		2. REPORT TYPE Final Report		3. DATES COVERED (From - To) 24 Sep 2014 – 11 Dec 2017	
4. TITLE AND SUBTITLE Modeling & Simulation for Particle Radiation Damage to Electronic and Opto-Electronic Devices				5a. CONTRACT NUMBER FA9453-14-1-0248	
				5b. GRANT NUMBER	
				5c. PROGRAM ELEMENT NUMBER 62601F	
6. AUTHOR(S) Sanjay Krishna				5d. PROJECT NUMBER 4846	
				5e. TASK NUMBER PPM00019212	
				5f. WORK UNIT NUMBER EF123126	
7. PERFORMING ORGANIZATION NAME(S) AND ADDRESS(ES) AND ADDRESS(ES) University of New Mexico 1700 Lomas Blvd. NE Albuquerque, NM 87106				8. PERFORMING ORGANIZATION REPORT NUMBER	
9. SPONSORING / MONITORING AGENCY NAME(S) AND ADDRESS(ES) Air Force Research Laboratory Space Vehicles Directorate 3550 Aberdeen Ave. SE Kirtland AFB, NM 87117-5776				10. SPONSOR/MONITOR'S ACRONYM(S) AFRL/RVSW	
				11. SPONSOR/MONITOR'S REPORT NUMBER(S) AFRL-RV-PS-TR-2018-0001	
12. DISTRIBUTION / AVAILABILITY STATEMENT Approved for public release; distribution is unlimited.					
13. SUPPLEMENTARY NOTES					
14. ABSTRACT In this effort, we have undertaken fundamental studies on vertical transport in an antimonide-based semiconductor superlattice structure. For this purpose, we used theoretical expressions based on Hovel model to extract the minority carrier diffusion length of a unipolar nBp type-II superlattice (T2SL) mid-wave infrared detector. Combining these results with the lifetime via Time-Resolved Photoluminescence (TRPL) data, we were able to additionally determine the minority vertical mobility and diffusivity, providing a comprehensive picture of vertical transport characteristics of the excited carrier in the nBp T2SL detectors. Finally, we performed dark current modeling and investigated the dominant dark current mechanisms at different temperatures. Our next step is to investigate the origin, types, and effects of radiation damage on this structure.					
15. SUBJECT TERMS Unipolar barrier infrared detectors, Dark current density, Quantum efficiency, Minority carrier lifetime, Minority carrier diffusion length, Type-II strained layer superlattice, Mid-wave infrared					
16. SECURITY CLASSIFICATION OF:			17. LIMITATION OF ABSTRACT	18. NUMBER OF PAGES	19a. NAME OF RESPONSIBLE PERSON
a. REPORT Unclassified	b. ABSTRACT Unclassified	c. THIS PAGE Unclassified			Christian Morath
			Unlimited	24	19b. TELEPHONE NUMBER (include area code)

(This page intentionally left blank)

TABLE OF CONTENTS

Section	Page
List of Figures	ii
Acknowledgments and Disclaimer	iv
1.0 SUMMARY	1
2.0 INTRODUCTION	1
3.0 METHODS, ASSUMPTIONS, AND PROCEDURES	2
3.1 Materials	2
3.2 Quantum Efficiency Modeling	3
3.3 Dark Current Modeling.....	5
4.0 RESULTS AND DISCUSSION	6
4.1 Quantum Efficiency Measurement and Modeling.....	6
4.2 Dark Current Modeling.....	10
5.0 CONCLUSIONS	12
REFERENCES	13
LIST OF ACRONYMS	14

LIST OF FIGURES

Figure		Page
1	(Left) Design Structure of the nBp T2SL Photodetector. (Right) Calculated Equilibrium Band Alignment of the nBp Structure	2
2	Schematic of the Device Dross-section for the nBp Diode.....	3
3	Absorption Coefficient at Different Operating Temperatures.....	7
4	(Left) QE at Zero Applied Bias, and (Right) QE at 200 mV Applied Bias, for 80 K, 120 K, and 150 K.	8
5	Comparison Between Experimental (Solid Lines) and Calculated (Dashed lines) QE Spectra for the nBp Photodetector at $V = 0.2$ V for $T = 80$ K, 120 K, and 150 K	9
6	Measured (Circle) and Simulated (Solid Line) Dark Current Density at 80K 120K, and 150K	11
7	Different Dark Current Mechanisms, the Total Simulated, and Experimentally Measured Dark Current Density for $T=80$ K, 120K, and 150K	11

ACKNOWLEDGMENTS

This material is based on research sponsored by Air Force Research Laboratory under agreement number FA9453-14-1-0248. The U.S. Government is authorized to reproduce and distribute reprints for Governmental purposes notwithstanding any copyright notation thereon.

DISCLAIMER

The views and conclusions contained herein are those of the authors and should not be interpreted as necessarily representing the official policies or endorsements, either expressed or implied, of Air Force Research Laboratory or the U.S. Government.

(This page intentionally left blank)

1.0 SUMMARY

We present a model for the spectral external quantum efficiency (EQE) to extract the minority carrier diffusion length (L_n) of a unipolar nBp InAs/GaSb Type-II superlattice (T2SL) mid-wave infrared (MWIR) detector. The detector consists of a 4 μm thick p -doped 10 monolayer (ML) InAs/10ML GaSb superlattice (SL) absorber with a 50% cut-off wavelength of 5 μm at 80 K and zero bias. The n -type doped InAs/AlSb SL barrier in the structure was included to reduce the generation-recombination dark current. By fitting the experimentally measured EQE data to the theoretically calculated quantum efficiency (QE) based on the solution of the drift-diffusion equation, the p -type absorber was found to have $L_n = 10 \pm 0.5 \mu\text{m}$ at 80K, and $L_n = 12 \pm 0.5 \mu\text{m}$ at 120K and 150K. We performed the absorption coefficient measurement at different temperatures of interest. Also, we estimated the reduced background concentration and the built-in potential by utilizing a capacitance-voltage measurement technique. We used time-resolved-photoluminescence (TRPL) to determine the lifetime at 80K. With the result of the model and the lifetime measurement, we calculated the diffusion coefficient and the mobility in the T2SL detector at various temperatures. Also, we studied the behavior of different dark current mechanisms by fitting the experimentally measured and simulated dark current density under different operating temperatures and biases.

2.0 INTRODUCTION

Semiconductor superlattices with type-II band alignment have been shown to be versatile materials for their applications in infrared (IR) optoelectronic devices. Type-II Superlattice (T2SL) based detectors were the focus of research in the last couple of decades with promising improvements demonstrated in their manufacturing, fabrication, and performance. However, the theoretically predicted advantages have not been achieved yet in these structures because of a high level of dark current. Different design structures using heterostructures and including a higher band-gap barrier have been proposed to reduce the dark current while leaving the photo-generated carriers unimpeded [1]. On the other hand, the effect of the physical phenomenon such as transport mechanisms and its relation to design and growth parameters in T2SLs are still unknown. Transport through the SL growth layers (i.e., vertical transport) has especially high importance in the design of IR detectors, since the carrier conduction via this path is the typical mode of operation and it affects the collection efficiency in the device.

Different groups have investigated transport in T2SLs using different theoretical and experimental techniques [2-7]. With the help of different semi-parametric modeling techniques, these methods can contribute to characterize the drift and diffusion parameters. Among these methods, the spectral QE measurement has proved useful in investigating the effect of different design parameters, such as absorber thickness [5] and background doping [7] on the performance of the T2SL IR detectors.

In this technical report, we report the result of spectral QE modeling on an InAs/GaSb T2SL *nBp* detector incorporating a hole-barrier (h-barrier). The analytical expressions derived for quantum efficiency of *pn* junction photodetectors by Hovel [8] have been utilized to extract different transport parameters in the model. Capacitance-voltage characterization has been performed to obtain information about the built-in potential and reduced carrier concentration. Also, TRPL has been measured to estimate the lifetime in the material at 80 K. Moreover, we used the dark current modeling to evaluate the performance of the photodiode and determine different parameters, such as reduced effective mass, trap energy states, and concentration of the material.

3.0 METHODS, ASSUMPTIONS, AND PROCEDURES

3.1 Materials

In this work, we studied a MWIR T2SL heterostructure as illustrated in Figure 1. The structure was grown by solid source molecular beam epitaxy on a GaSb: Te (001) epi-ready substrate. The epi structure consists of a 250-nm non-intentionally doped GaSb buffer layer, followed by 1.5- μm thick *p*-doped ($5 \times 10^{17} \text{ cm}^{-3}$) bottom contact layer with a bandgap of 0.250 eV composed of 10 ML InAs/10 ML GaSb T2SL, a 4- μm thick *p*-doped ($5 \times 10^{16} \text{ cm}^{-3}$) absorber region composed of a 10 ML InAs /10 ML GaSb T2SL with a bandgap of 0.250 eV , a 250-nm thick lightly *n*-doped ($5 \times 10^{15} \text{ cm}^{-3}$) hole barrier (h-Barrier) with a bandgap of 0.650 eV composed of a 12 ML InAs/ 6 ML AlSb T2SL, and a 200-nm thick *n*-doped ($5 \times 10^{17} \text{ cm}^{-3}$) top contact layer with a bandgap of 0.360 eV composed of a 5 ML InAs/ 4 ML GaSb T2SL. The h-Barrier helps minimize the dark current generation, while at the same time allows photo-generated carriers to flow unimpeded to the contacts. We then processed the wafer into variable area single-pixel devices for further characterizations, the details of which have been discussed in Reference 9.

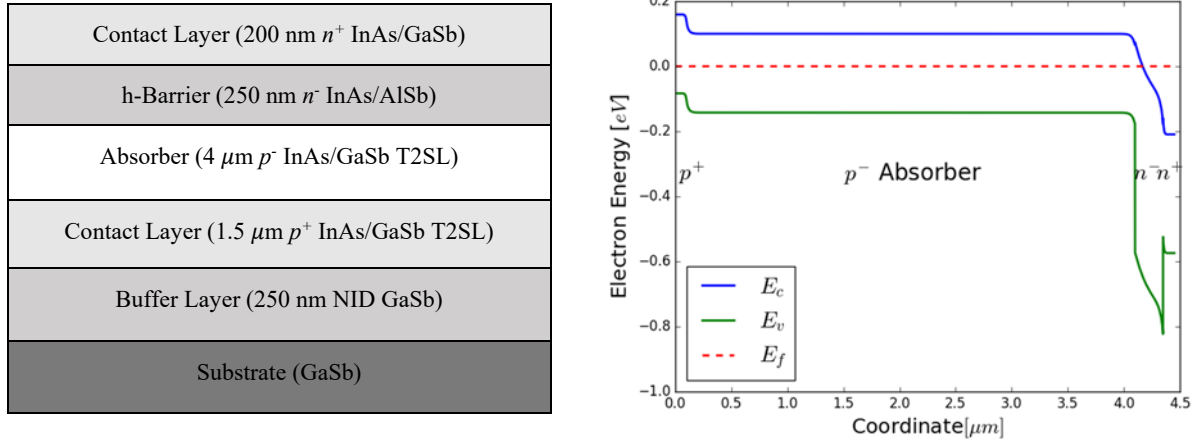


Figure 1. (Left) Design Structure of the *nBp* T2SL Photodetector. (Right) Calculated Equilibrium Band Alignment of the *nBp* Structure

3.2 Quantum Efficiency Modeling

We have used a simple analytical model based on the Hovel expressions [8] to simulate the quantum efficiency in an nBp photodiode under optical illumination. This model has been tested on T2SLs, previously [5],[7],[10]. It is based on some simplifying assumptions that when fulfilled, it can be used as the first principle approximation for estimating a device's performance. These assumptions include: 1) Low-level injection: $n_{p0} \ll p_{p0}$ (p -type) or $n_{n0} \gg p_{n0}$ (n -type), 2) Uniform material: spatially invariant parameters, 3) Zero excess minority carriers at the depletion edges, 4) Uniform absorption coefficient (α) in each region of the diode, 5) Negligible recombination in the depletion region, and 6) Negligible majority carrier current. Using these assumptions, the nonlinear drift-diffusion equation can be solved, and the analytical solution for quantum efficiency in n -, p -, and depletion regions can be obtained using a set of boundary conditions [8]. Figure 2 shows the cross-section of the photodiode that we used in this model. The n -region of the diode consists of the top-contact layer and the h -barrier with different absorption properties. The p -region consists of the absorber region and the bottom contact. W is the thickness of depletion region, x_j is the junction depth, H is the total thickness of the diode, x_n and x_p are the depletion width in n - and p -regions, respectively.

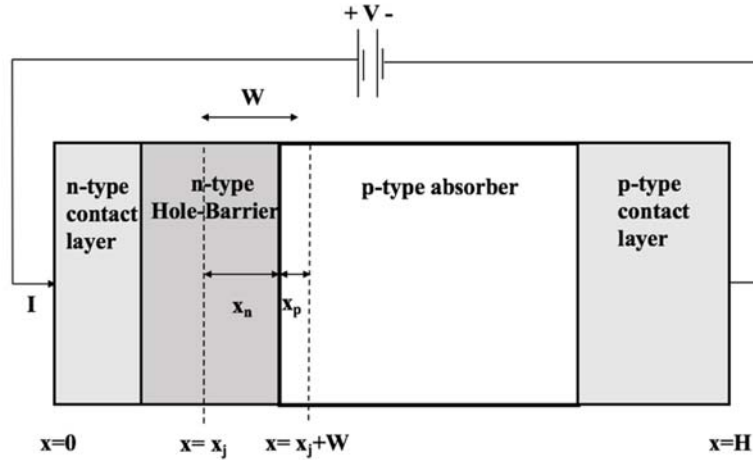


Figure 2. Schematic of the Device Cross-Section for the nBp Diode

Assuming the light is incident on the n -side of the photodiode, the drift-diffusion equation for the minority electron of the p -type material can be written as

$$D_n \frac{\partial^2(\delta n)}{\partial x^2} + \mu_n E \frac{\partial(\delta n)}{\partial x} + g - \frac{\delta n}{\tau_{n0}} = \frac{\partial(\delta n)}{\partial t} \quad (1)$$

where D_n is the electron diffusion coefficient, μ_n is the electron mobility, E is the applied electric field, g is the generation rate, and τ_{n0} is the electron recombination lifetime. Upon optical illumination, electron-hole pairs (EHPs) are produced in the material. The EHPs then contribute to the current measured in the external circuit if they reach the depletion edges before they recombine, from where they will be swept out by the electric field.

Approved for public release; distribution is unlimited.

The generation rate associated with the optical excitation in the device is given by [8].

$$g(\lambda) = \alpha(\lambda)\Phi(\lambda)[1 - R(\lambda)]e^{-\alpha(\lambda)x}, \quad (2)$$

where $\alpha(\lambda)$ is the wavelength-dependent absorption coefficient of the material, $\phi(\lambda)$ is the total number of incident photons per unit area per second per unit bandwidth, and the $R(\lambda)$ is the power reflectivity.

Under steady state conditions, and considering zero-applied electric field, Equation (1) can be solved using two boundary conditions for each region: (a) A perfect collector condition at the junction edge ($p_n - p_{n0} = 0$, for the p -region), and (b) The boundary between the material and vacuum, at which the surface recombination occurs, characterized by its recombination velocity S with the dimension of $\text{cm}\cdot\text{s}^{-1}$ ($D_p \frac{\delta(p_n - p_{n0})}{\delta x} = S_p(p_n - p_{n0})$, for the p -region). The result will be the density of minority carriers $\delta n(x)$, in the p -side of the photodiode, which is used to calculate the diffusion photocurrent densities (J_{ph}). The same calculation can be done for the minority holes in the n -region. The total QE in the device can then be written as

$$QE = \frac{1}{q\Phi} (J_{ph-n} + J_{ph-SCR} + J_{ph-p}) = QE_n + QE_{SCR} + QE_p. \quad (3)$$

The quantum efficiency components, QE_p , QE_n and QE_{SCR} (corresponding to the photocarrier generation in the p -, n -, and space-charge regions, respectively) can be defined as

$$QE_p = (1 - R) \frac{\alpha_p L_n}{\alpha_p^2 L_n^2 - 1} e^{-[\alpha_n x_j + \alpha_{nb} W_1 + \alpha_p W_2]} \times \left[\alpha_p L_n - \frac{L_n \frac{S_n}{D_n} \left[\cosh\left(\frac{x'}{L_n}\right) - e^{-\alpha_p x'} \right] + \alpha_p L_n e^{-\alpha_p x'} + \sinh\left(\frac{x'}{L_n}\right)}{\left[L_n \frac{S_n}{D_n} \sinh\left(\frac{x'}{L_n}\right) + \cosh\left(\frac{x'}{L_n}\right) \right]} \right], \quad (4)$$

where, α_n , α_{nb} and α_p are the absorption coefficients of the n -type top-contact, the n -type h-barrier, and the p -type absorber, respectively. x' is the thickness of the p -region, L_n is the electron diffusion length, and S_n/D_n is the electron surface recombination velocity to diffusion coefficient ratio.

$$QE_n = (1 - R) \frac{\alpha_n L_p}{\alpha_n^2 L_p^2 - 1} \left[\frac{\alpha_n L_p + L_p \frac{S_p}{D_p} e^{-\alpha_n x_j} \left[L_p \frac{S_p}{D_p} \cosh\left(\frac{x_j}{L_p}\right) + \sinh\left(\frac{x_j}{L_p}\right) \right]}{\left[L_p \frac{S_p}{D_p} \sinh\left(\frac{x_j}{L_p}\right) + \cosh\left(\frac{x_j}{L_p}\right) \right]} - \alpha_n L_p e^{-\alpha_n x_j} \right], \quad (5)$$

where x_j is the junction depth, L_p is the hole diffusion length, and S_p/D_p is the hole surface recombination velocity to diffusion coefficient ratio.

$$QE_{SCR} = (1 - R) e^{-\alpha_n x_j} [1 - e^{-(\alpha_{nb} W_1 + \alpha_p W_2)}], \quad (6)$$

where W_1 and W_2 are the depletion widths in the n - and p -region, respectively.

The total quantum efficiency is dependent on the absorption coefficient (α), the background doping concentration, the minority-carrier diffusion lengths (L_n and L_p), and the surface velocity recombination to diffusion coefficient ratios (S/D at the two interfaces). The latter can be assumed to be zero since it does not change the shape of the curve. However, it can affect the absolute magnitudes when the junction depth of the diode and the effective minority carrier diffusion length become comparable [7]. With this assumption, the results should be considered as a lower bound on L_n [5]. Other methods, such as Electron Beam Induced Current (EBIC) can be used to extract S and L simultaneously and to verify the results of this model. So, by choosing L as a fitting parameter, while providing the information about other parameters, one can fit the model to the experimentally measured quantum efficiency to extract L .

3.3 Dark Current Modeling

We also performed dark current modeling to characterize the photodiode further. For this purpose, we fit the experimentally measured dark current to analytically simulated dark current. Assuming a neutral center and a constant electric field across the depletion region, and a triangular barrier, the simulated dark current is expressed as the sum of the diffusion current (I_{diff}), generation-recombination current (I_{gr}), tunneling current (including the trap-assisted (I_{TAT}) and band-to-band components (I_{BTB})) as [11-12].

$$I_{diff} = A\sqrt{qk_B T} \left[\frac{n_i^2}{N_A} \sqrt{\frac{\mu_e}{\tau_e}} \tanh\left(\frac{x_p}{L_p}\right) \right] \left(\exp\left(\frac{qV_i}{k_B T}\right) - 1 \right) \quad (7)$$

$$I_{gr} = \frac{2An_i W k_B T}{(V_{bi} - V_i)\tau_{gr}} \sinh\left(\frac{-qV_i}{2k_B T}\right) f(b) \quad (8)$$

$$I_{TAT} = \frac{Aq^2 m_t M^2 N_t V_i}{8\pi\hbar^3 (E_g - E_t)} \exp\left(\frac{-4\sqrt{2m_t(E_g - E_t)^3}}{3qE\hbar}\right) \quad (9)$$

$$I_{BTB} = \frac{Aq^3 E V_i \sqrt{2m_{red}}}{4\pi^2 \hbar^2 \sqrt{E_g}} \exp\left(\frac{-4\sqrt{2m_{red}E_g^3}}{3qE\hbar}\right) \quad (10)$$

where A is the device area, q is the electron charge, k_B is the Boltzmann constant, T is the temperature, n_i is the intrinsic carrier concentration, N_A and N_D are the absorber's and barrier's doping concentrations, respectively, μ_e is the electron mobility, τ_e is the electron lifetime, V_i is the bias voltage, V_{bi} is the built-in potential, W is the depletion width, τ_{gr} is the generation-combination lifetime, \hbar is the Planck constant, m_t is the effective tunneling mass, N_t is the trap density, E_t is the trap energy location, measured from the valence band edge, M^2 is a matrix element associated with the trap potential, assumed to be 10^{-23} eV-cm^3 , E_g is the absorber's band gap, E is the electric field, m_{red} is the reduced effective mass and

$$f(b) = \begin{cases} \frac{1}{2\sqrt{b^2-1}} \ln(2b^2 + 2b\sqrt{b^2-1} - 1) & b > 1 \\ 1 & b = 1 \\ \frac{1}{\sqrt{1-b^2}} \tan^{-1}\left(\frac{\sqrt{1-b^2}}{b}\right) & b < 1 \end{cases} \quad (11)$$

where, $b = e^{\frac{-qV_i}{2k_B T}}$.

The total voltage (V_{app}) applied to the structure can be expressed as the sum of the voltage drops on an ohmic series resistance and the effective applied bias on the depletion region

$$V_{app} = V_i + R_s I, \quad (12)$$

for which we extracted R_s from the forward bias voltage region of the differential resistance-voltage characteristic to be 0.5 Ohms for all temperatures of interest. We estimated V_{bi} to be 0.16 V from capacitance-voltage (C-V) measurement. Also, we defined the depletion widths in the barrier and absorber, and the electric field at the barrier-absorber heterojunction as [12-13].

$$W_n^2 = \frac{2\epsilon_n\epsilon_p N_A (V_{bi} - V_i)}{q N_A (\epsilon_n N_D + \epsilon_p N_A)}, \quad (13)$$

$$W_p^2 = \frac{2\epsilon_n\epsilon_p N_D (V_{bi} - V_i)}{q N_D (\epsilon_n N_D + \epsilon_p N_A)}, \quad (14)$$

$$E = \frac{\epsilon_n + \epsilon_p}{2} \sqrt{\frac{2q(V_{bi} - V_i) N_A N_D}{\epsilon_n \epsilon_p (\epsilon_p N_A + \epsilon_n N_D)}}. \quad (15)$$

4.0 RESULTS AND DISCUSSION

4.1 Quantum Efficiency Measurement and Modeling

The knowledge of the wavelength dependence of the absorption coefficient ($\lambda(\alpha)$) is required to extract diffusion length from the spectral quantum efficiency model. In this work, we determined the absorption coefficient through IR transmission measurements using a Fourier transform infrared (FTIR) spectrometer. The T2SL epi-layers were etched off to different thicknesses on three separate pieces, in which the top contact, the h-barrier, and the absorber were removed, respectively, to measure the transmission spectra of each layer separately. The samples were mounted side-by-side in the cryostat with ZnS windows and transmission spectra at 80 K, 120 K, and 150 K were measured using reflective optics. The same sized apertures on each sample were used in the measurement to ensure the identical radiant flux for each sample. The result of the transmission at each layer was compared directly to the transmission of its underlying layers. The absorption coefficients for the top-contact, the h-barrier, and the absorber were then calculated using the model [11],[14] and the effect of the reflection in normal incidence configuration was considered in the calculation.

Figure 3 shows the result of the measured absorption coefficient of the absorber layer with the thickness of 4 μm at 80 K, 120 K, and 150 K, which increases slightly with temperature.

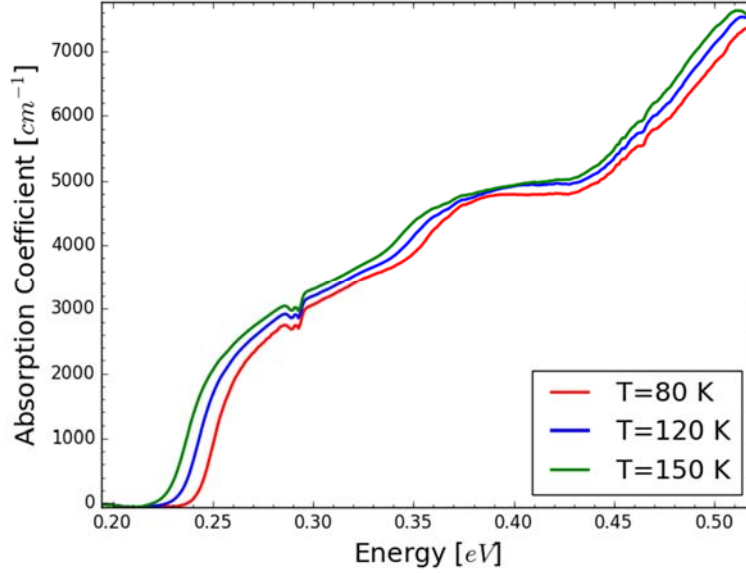


Figure 3. Absorption Coefficient Under Different Operating Temperatures

For quantum efficiency measurements, we used a standard setup consisting of a calibrated blackbody, narrow band filters (centered at 3.4 and 4.5 μm), a current pre-amplifier, and a lock-in amplifier. Measurements were performed using front-side illumination geometry with no anti-reflection coating. The results for quantum efficiency at 3.4 and 4.5 μm were used to calibrate the spectral photoresponse, which was obtained using an FTIR spectrometer and was normalized to a reference detector's response.

Figure 4 shows the results of the quantum efficiency under zero and 200 mV applied bias at 80 K, 120 K, and 150 K. The insets show the trend of the QE at $\lambda = 4.5 \mu\text{m}$ with temperature. The device used for this measurement was 500 μm in size. The CO_2 absorption at 0.295 eV is visible in the experimental data. The dependence of quantum efficiency with applied bias was also measured at the same temperatures. It revealed that the turn-on bias increases with temperature, most probably due to the presence of a barrier at the heterojunction interface, which changes with the temperature. As a result, the quantum efficiency at 0 V decreases with temperature. However, it stays nearly constant at 200 mV bias. For this reason, the data for 200 mV applied bias was chosen for use in the model. The inclusion of bias affects the simulated quantum efficiency only through changing the depletion region width.

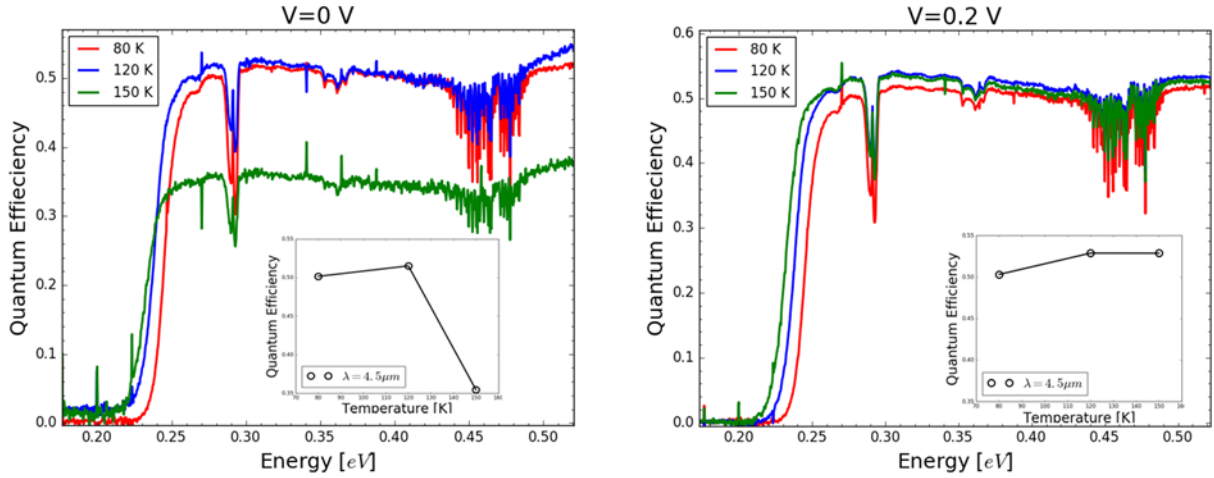


Figure 4. (Left) QE at Zero Applied Bias, and (Right) QE at 200 mV Applied Bias, for 80 K, 120 K, and 150 K.

The fitting of the simulated and measured spectral quantum efficiency at various temperatures was done using the diffusion length as the fitting parameter. For this purpose, we used the spectral area primarily around the band edge as the main focus of the fitting, where the absorber (*p*-region) has the most profound effect. It should be noted that we neglected the contribution of the QE_n and QE_{SCR} in the simulation since they are mostly effective at the higher energy regions of the quantum efficiency spectra.

Figure 5 shows the comparison of the measured and simulated spectral quantum efficiency at three different temperatures under applied bias of 200 mV. The simulated quantum efficiency is in good agreement with the experimental results in the region near the band edge. The difference at higher energy indicates that the carriers excited by the incoming radiation have some loss due to absorption in the top contact region. Also, other factors might be responsible such as the error in the absorption measurement used in the model.

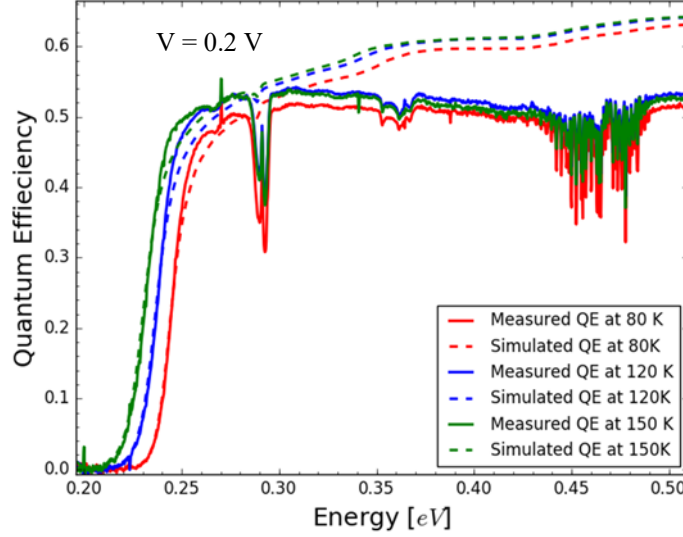


Figure 5. Comparison Between Experimental (Solid Lines) and Calculated (Dashed lines) QE Spectra for the *nBp* Photodetector at $V = 0.2$ V for $T = 80$ K, 120 K, and 150 K

We estimated the diffusion lengths that correspond to the best fits between experimental and calculated quantum efficiency. Moreover, we calculated the diffusion coefficient using the diffusion length and lifetime at each temperature. Having the diffusion coefficients, we also calculated the mobility at each temperature using the Einstein relation ($\mu_n = \frac{D_n q}{k_B T}$). We used the lifetime from TRPL measurements for the calculation at 80 K, while the lifetime at other temperatures was inferred from the dark current modeling as will be discussed later. Table 1 summarizes the results of different parameters for several operating temperatures at $V_{\text{applied}} = 0.2$ V.

Table 1. A Summary of Different Transport Properties Extracted from the QE Model

Temperature [K]	Diffusion Length [μm]	Diffusion Coefficient [$\text{cm}^2 \text{s}^{-1}$]	Mobility [$\text{cm}^2 \text{V}^{-1} \text{s}^{-1}$]	Lifetime [ns]
80	10	33.33	4826.08	30
120	12	53.33	5149.75	27
150	12	60.00	4637.68	24

Depletion Width (W): $0.3 \mu\text{m}$
Junction Depth (x_j): $0.28 \mu\text{m}$
SL Thickness (H): $5.95 \mu\text{m}$

4.2 Dark Current Modeling

For this part, we used m_{red} , m_t , E_t , N_t , n_i , N_A , and N_D as the fitting parameters in equations (7-10). We used the TRPL result for τ_e and τ_{gr} , which were taken to be similar (τ), at 80 K. We then used τ as a fitting parameter at higher temperatures. Table 2 summarizes the results for 80 K, 120 K, and 150 K. It is evident that the trap state's energy increases with temperature. Moreover, τ decreases gradually with temperature. All the other parameters except for n_i were fit using 80 K data and were kept the same for other temperatures.

Table 2. Summary of Different Fitting Parameters from Dark Current Modeling

Temperature [K]	80	120	150
m_{red} / m_0	0.011	0.011	0.011
$N_t [\text{cm}^{-3}]$	1×10^{11}	1×10^{11}	1×10^{11}
$E_t / E_{g\text{absorber}}$	0.800	0.845	0.865
m_t / m_0	0.055	0.055	0.055
$\tau [\text{ns}]$	30	27	24
$n_i [\text{cm}^{-3}]$	2×10^{12}	7×10^{12}	5.5×10^{13}
$N_A [\text{cm}^{-3}]$	3.9×10^{16}	3.9×10^{16}	3.9×10^{16}
$N_D [\text{cm}^{-3}]$	7.2×10^{15}	7.2×10^{15}	7.2×10^{15}

Figure 6 shows the variation of measured and simulated dark current densities with applied bias at different temperatures. Also, Figure 7 demonstrates various dark current mechanisms versus bias at 80 K, 120 K, and 150 K. The device used for the dark current modeling was 200 μm in size. Under all operating temperatures, we found I_{TAT} and I_{BTB} to be dominant at higher biases, while I_{BTB} was leading at 80 K and this fact was used to determine the reduced effective mass in the material. On the other hand, I_{diff} and I_{gr} contributions were more significant in the lower bias regime with I_{diff} leading at 150 K.

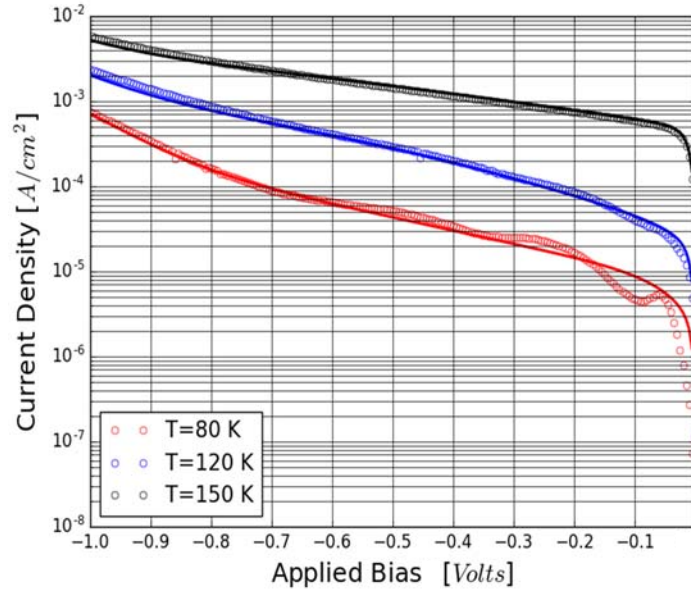


Figure 6. Measured (Circle) and Simulated (Solid Line) Dark Current Density at 80K, 120K, and 150K

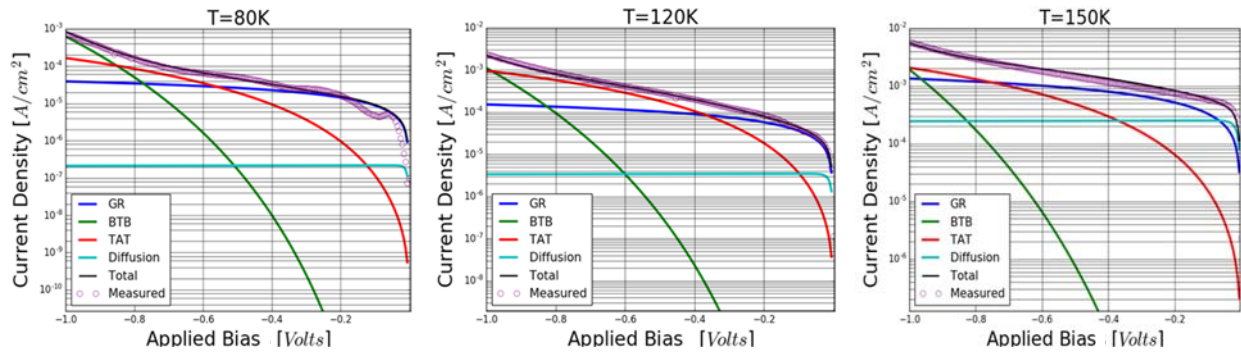


Figure 7. Different Dark Current Mechanisms, the Total Simulated, and Experimentally Measured Dark Current Density for T=80K, 120K, and 150K

5.0 CONCLUSIONS

In summary, we report the result of a set of analytical models to evaluate the performance of T2SL detectors based on the InAs/GaSb T2SL nBp photodiode, including spectral quantum efficiency and dark current modeling. The quantum efficiency model, based on the Hovel expressions was presented. We measured the absorption coefficient at different temperatures and used its result to fit the model to the experimental quantum efficiency data and to extract the diffusion length of the minority electrons in the absorber layer under applied bias of 200 mV. We found the diffusion lengths to be longer than the absorber thickness at all temperature of interest. We used TRPL measurements to estimate the lifetime at 80 K and calculated the diffusion coefficient and mobility at different temperatures. Moreover, we performed dark current modeling to investigate the dominant dark current mechanism at different bias regimes and temperatures. Various parameters such as the reduced effective mass, trap energy state, trap concentration, and the lifetime at all the operating temperatures was determined.

REFERENCES

- [1] Martyniuk P., *et al.*, “Barrier infrared detectors,” *Opto-Electronics Rev.*, vol. 22, no. 2, pp. 127–146, 2014.
- [2] Umana-Membreno G. A., *et al.*, “Vertical minority carrier electron transport in p-type InAs/GaSb type-II superlattices,” *Appl. Phys. Lett.*, vol. 101, no. 25, pp. 1–5, 2012.
- [3] Li J. V., *et al.*, “Minority carrier diffusion length and lifetime for electrons in a type-II InAs/GaSb superlattice photodiode,” *Appl. Phys. Lett.*, vol. 85, no. 11, pp. 1984–1986, 2004.
- [4] Olson B. V., *et al.*, “All-optical measurement of vertical charge carrier transport in mid-wave infrared InAs/GaSb type-II superlattices,” *Appl. Phys. Lett.*, vol. 102, p. 202101, 2013.
- [5] Aifer E. H., *et al.*, “W-structured type-II superlattice long-wave infrared photodiodes with high quantum efficiency,” *Appl. Phys. Lett.*, vol. 89, no. 5, pp. 1–4, 2006.
- [6] Mou S., *et al.*, “Quantum Efficiency Analysis of InAs/GaSb Type-II Superlattice Photodiodes,” *Quantum Electron. IEEE J.*, vol. 45, no. 6, pp. 737–743, 2009.
- [7] Giard E., *et al.*, “Quantum efficiency investigations of type-II InAs/GaSb midwave infrared superlattice photodetectors,” *J. Appl. Phys.*, vol. 116, no. 4, pp. 1–7, 2014.
- [8] Hovel H. J., *Semiconductors and semimetals. Volume 11. Solar cells*, New York, San Francisco, and London, Academic Press, 1975.
- [9] Kazemi A., *et al.*, “High quantum efficiency mid-wavelength infrared superlattice photodetector,” *Proc. SPIE*, vol. 10177, p. 101771M, 2017.
- [10] Wu H., *et al.*, “Performance analysis of an N-structure type-II superlattice photodetector for long wavelength infrared applications,” *J. Alloys Compd.*, vol. 684, pp. 663–668, 2016.
- [11] Nguyen J., *et al.*, “Dark current analysis of InAs/GaSb superlattices at low temperatures,” *Infrared Phys. Technol.*, vol. 52, no. 6, pp. 317–321, 2009.
- [12] Martyniuk P., *et al.*, “Performance modeling of MWIR InAs/ GaSb/ B–Al(0.2) Ga(0.8)Sb type-II superlattice nBn detector,” *Semicond. Sci. Technol.*, vol. 27, no. 5, p. 55002, 2012.
- [13] Sze S. M. and Ng K. K., *Physics of Semiconductor Devices*, 3rd Edition, Wiley, 2007.
- [14] Ariyawansa G., *et al.*, Duran J. M., Scheihing J. E., and Eismann T., “Absorption characteristics of mid-wave infrared type-II superlattices,” *Proc. SPIE*, vol. 9070, p. 90701J, 2014.

LIST OF ACRONYMS

C-V	Capacitance-Voltage
EBIC	Electron Beam Induced Current
EHP	Electron-hole Pairs
EQE	External Quantum Efficiency
FTIR	Fourier Transform Infrared
H-barrier	Hole-barrier
IR	Infrared
ML	Monolayer
MWIR	Mid-wave Infrared Detector
QE	Quantum Efficiency
SL	Superlattice
T2SL	Type-II Superlattice
TRPL	Time-Resolved Photoluminescence

DISTRIBUTION LIST

DTIC/OCP 8725 John J. Kingman Rd, Suite 0944 Ft Belvoir, VA 22060-6218	1 cy
AFRL/RVIL Kirtland AFB, NM 87117-5776	1 cy
Official Record Copy AFRL/RVSW/Christian Morath	1 cy

Approved for public release; distribution is unlimited.

(This page intentionally left blank)